Schweizerischer Erdbebendienst
Service Sismologique Suisse
Servizio Sismico Svizzero
Swiss Seismological Service

ETH zürich

SITE CHARACTERIZATION REPORT

SFRU: Fribourg (FR) - Université

Clotaire Michel, Paolo Bergamo, Agostiny Lontsi, Manuel Hobiger, Donat Fäh

Last Modification: 26th October, 2017

Schweizerischer Erdbebendienst (SED)
Service Sismologique Suisse
Servizio Sismico Svizzero
Servizi da Terratrembels Svizzer

ETH Zurich
Sonneggstrasse 5
8092 Zurich
Schweiz
clotaire@sed.ethz.ch

Contents

Summary

The new station SFRU was installed in the Fribourg (FR) University campus and the installation site has been characterized. We performed passive and active seismic measurements that successfully allowed us to retrieve 1D velocity profiles at the station site. The profiles show three layers of morainic and infra-morainic sediments: 2.5 m with a shear wave velocity of 200 m/s, about 8 m with 400 m/s and about 35 m with 750 m/s. Below these sediments, one finds Molasse rock with increasing velocity starting at 1300 m/s at 45 m depth. The clearest contrast occurs between the second and the third sediment layers, at about 10 m depth, corresponding to a peak at 10 Hz.
$V_{s,30}$ is 534 m/s and the site corresponds to ground type B in the Eurocode 8 (CEN, 2004) and in the SIA261 (SIA, 2014). The theoretical 1D SH transfer function computed from the inverted profiles shows an increasing amplification with frequency with a peak at 10 Hz reaching an amplification of a factor of 3.5. While this site can be considered as representative for the city of Fribourg, strong lateral variations are expected. More recordings at the station SFRU are however needed to validate this shear wave velocity profiles using Empirical Spectral Modelling.

1 Introduction

In the framework of the second phase of the Swiss Strong Motion Network (SSMNet) renewal project, a new station installation in the Fribourg (FR) University campus, close to the building of the Department of Mathematics was decided. It is located in the Swiss foreland, at the top of a molasse hill above the Sarine river (see Fig. 1). The new station went operational on 13 December 2016.

Figure 1: SFRU station during the array measurement, close to the building of the Department of Mathematics.

2 Geological setting

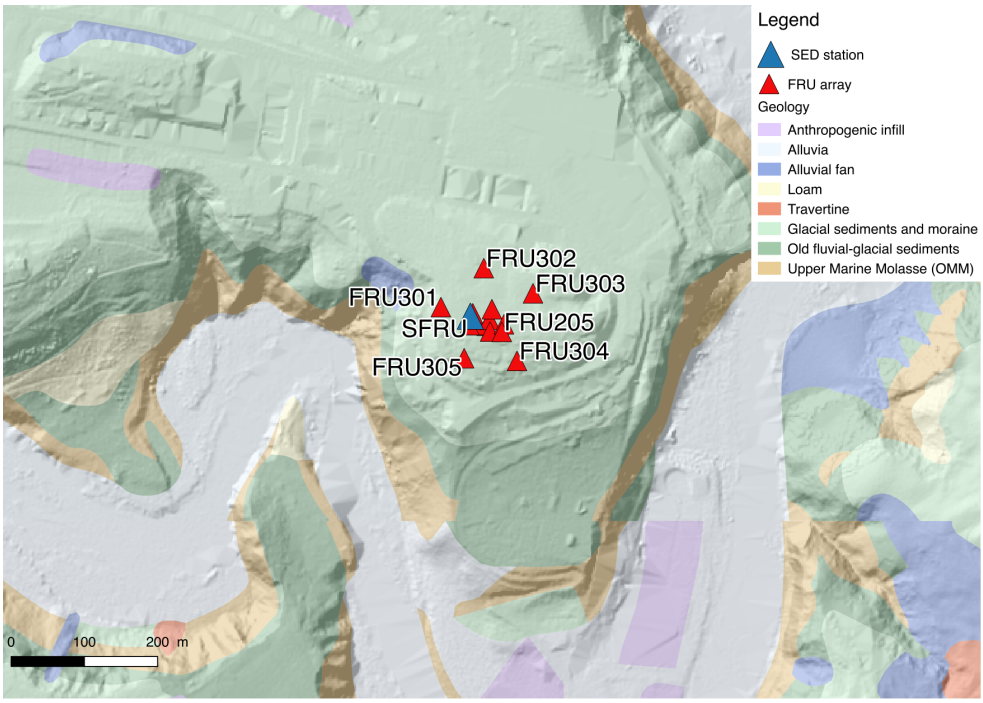

Figure 2: Simplified geological map of the area of the Pérolles University campus in Fribourg superimposed on a relief map (data: © 2017 swisstopo JD100042). The SED station SFRU and the passive array are displayed.

Fribourg is located in the Swiss foreland, on the Upper Marine Molasse (OMM, Burdigalian age) superimposed by morainic and fluvial-glacial sediments of various thickness and consolidation (Fig. 2). The study-site is located at the top of a hill above the Sarine gorges (steep topography) that display its geological profile. While the study site is located at 640 m altitude, the OMM follows the 600 m terrain line and old fluvial-glacial sediments the 610 m terrain line. One therefore expects about 30 m of moraine overlaying 10 m of old fluvial glacial sediments dominated by cemented gravels and the OMM at 40 m depth.
Based on information provided by the GeoMol website (`https://viewer.geomol.ch/webgui/`, last accessed Sept. 2017), the OMM is about 50 m thickness at this location. Below, one finds a thick layer of Molasse Grise de Lausanne (Lower Freshwater Molasse - USM) that could therefore be found at 90 m depth. However, the geological map does not show this layer in the Sarine gorges that are only 80 m deep. The interface with the Mesozoic rock is at about 2.5 km depth.
The site has been classified by the canton as ground type E (SIA261), as well as most of the city, but based on a former definition of the SIA261 ground types (SIA, 2003).

3 Site characterization using passive measurements

3.1 Measurements and data set

We investigated the local underground structure by passive seismic array measurements, which took place on March 31st, 2017. The layout of the passive seismic array is shown in Fig. 3.
The parameters of the array are given in Table 1. For these measurements 11 Nanometrics Centaur dataloggers named NR42 to NR49 and NR52 to NR54 and 14 Lennartz 3C 5 s seismometers were available. Each datalogger can record on 2 ports A (channels EH1, EH2, EH3 for Z, N, E directions) and B (channels EH4, EH5, EH6 for Z, N, E directions). Time synchronization is ensured by GPS. The sensors were placed on metal tripods. For better coupling with the ground, the tripods were placed in 10 cm deep holes, when possible.
The sensor coordinates were measured using a differential GPS device (Leica Viva GS10), including only a rover station and using the Real Time Kinematic technique provided by Swisstopo. It allowed in theory an absolute positioning with an accuracy better than few centimeters on the Swissgrid, but the presence of trees and buildings considerably decreased the precision here. While most of the points were measured with an accuracy better than 5 cm, points FRU201 and FRU205 had an accuracy between 10 and 20 cm, FRU305 of about 30 cm, FRU304 of about 50 cm and FRU103 of about 85 cm. This last point may be the only real issue for the processing, given that ring 1 it belongs to has a radius of 10 m (about 10% error).

Table 1: Characteristics of the passive seismic array measurements in Fribourg.

Array name	Number of sensors	Minimum interstation distance [m]	Aperture [m]	Recording time [min]
FRU	14	10	140	158

Figure 3: Layout of the passive array measurements at site SFRU. Array stations are in red and SFRU station in blue.

The largest time windows were extracted, for which all the sensors of the array were correctly placed and the GPS synchronization was ensured. The spectra are reasonably similar up to 10 Hz. FRU103 shows peaks at low frequency (0.3, 0.7 Hz), probably due to a local disturbance (power cable?). Harmonic disturbances are present at various frequencies and locations (4.2, 6.9, 7.5, 25 Hz...). The time traces are much disturbed by pedestrians (us) walking close to the stations.
Orientations of the sensors were checked by maximizing the correlation with the central station at low frequencies (Poggi et al., 2012b). Corrections lower than 6 ° were observed, but point FRU103 showed a strange distribution.

3.2 Single station measurements results

3.2.1 H/V curves

The H/V curves across the array are presented in Fig. 4. A first peak at 0.84 Hz is present on all recordings, as well as on all H/V recordings performed in the city. The observed variations are most probably related to picking uncertainties and not to actual variations in this layer, considering the wavelength the peak corresponds to. It corresponds probably to a deep interface within the Molasse rock, or with the basement.
Another peak at about 10 Hz at the array centre (FRU000 to FRU205) represent most probably the interface between the Quaternary and the Molasse rock. This contrast is not very strong considering that the amplitude in the H/V is low. The variations in the peak in the array centre are related to the picking uncertainty.
In the array, other peaks around 5 Hz can be seen at some points. At FRU202 and FRU301, the 6 Hz peak relates probably to the resonance of the Mathematics building of the University located close by and not to a geological feature. At FRU201, FRU305 and FRU305, the 4.5 Hz peak could not be interpreted.

Station FRU202 is the closest to station SFRU, as well as the existing point FRI101 from SED database measured in March 2016. They both clearly show these 3 peaks with amplitudes of 2.5 for the second and third. The fundamental peaks of FRU202 and FRI101 are slightly different (0.85 vs 0.94 Hz) maybe due to variation in the wavefield. Data from station SFRU were also analysed using H/V ratios (Fig. 5). They are covered by instrumental noise up to 3 Hz so that the fundamental peak cannot be seen. However, a peak at 5.8 Hz and the peak at 10.9 Hz are clear. The second peak is probably due to contamination of soil-structure interaction from the nearby building.

In the city, existing data from single station measurements are represented in Fig. 6 and Fig. 7. They confirm the existence of the deep resonance, while observed variations are due to picking uncertainties and cannot be interpreted (wavelength of 1.5 to 2 km). The second peak is generally at high frequency, while lower values (about 3-4 Hz) are observed North of the Pérolles campus, in the direction of the train station, where deeper sediments can be seen from the boreholes of the local geology map.

Moreover, various methods to compute H/V ratios are compared at point FRU000 in Fig. 8, in which the classical methods were divided by $\sqrt{2}$ to correct for the Love waves contribution (Fäh et al., 2001). The 3C FK analysis (Capon method, see section 3.3) matches relatively well H/V analysis when using the maxima picked on the radial component, but shows much lower values that do not match the H/V when using the maxima picked on the vertical component. The WaveDec results also show comparable results with the H/V analysis. Both FK with radial and WaveDec show a clear peak around 10 Hz. WaveDec shows that there is no singularity at the 10 Hz peak and the ellipticity remains retrograde. In the high frequency range, WaveDec active shows that there is a singularity around 26 Hz corresponding to a shallow layer (about 2 m).

The fundamental peak at the SFRU station is therefore at about 0.9 Hz, with a peak amplitude around 2 and the peak related to the Quaternary to rock interface at 10.9 Hz with a peak amplitude of 2.5.

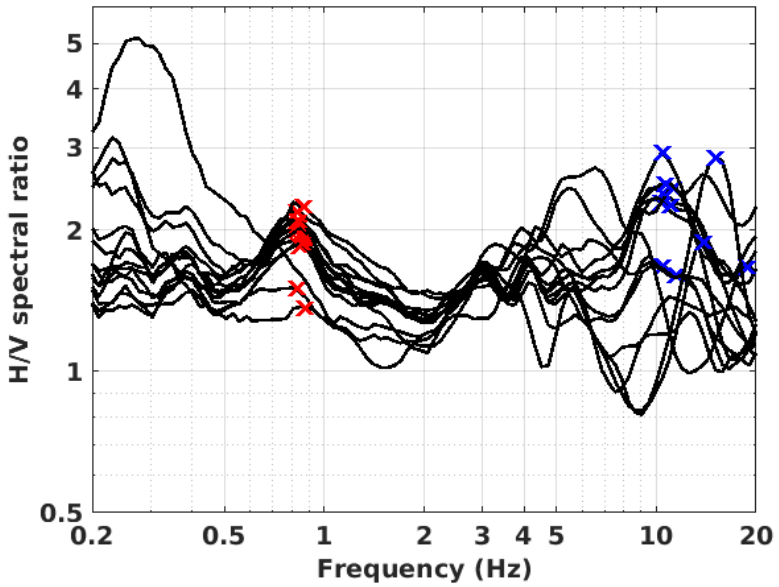

Figure 4: Comparison of H/V spectral ratios (time-frequency analysis code V. Poggi) between the different points of the arrays, including picking of the first and last resonance peaks.

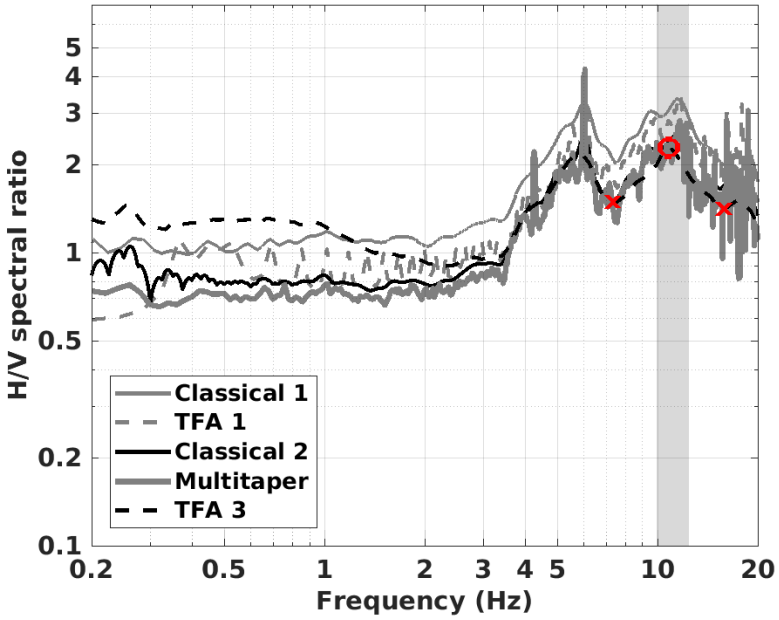

Figure 5: H/V spectral ratios using different codes with data from station SFRU. Note that below 3 Hz, the signal is dominated by instrumental noise and cannot be interpreted.

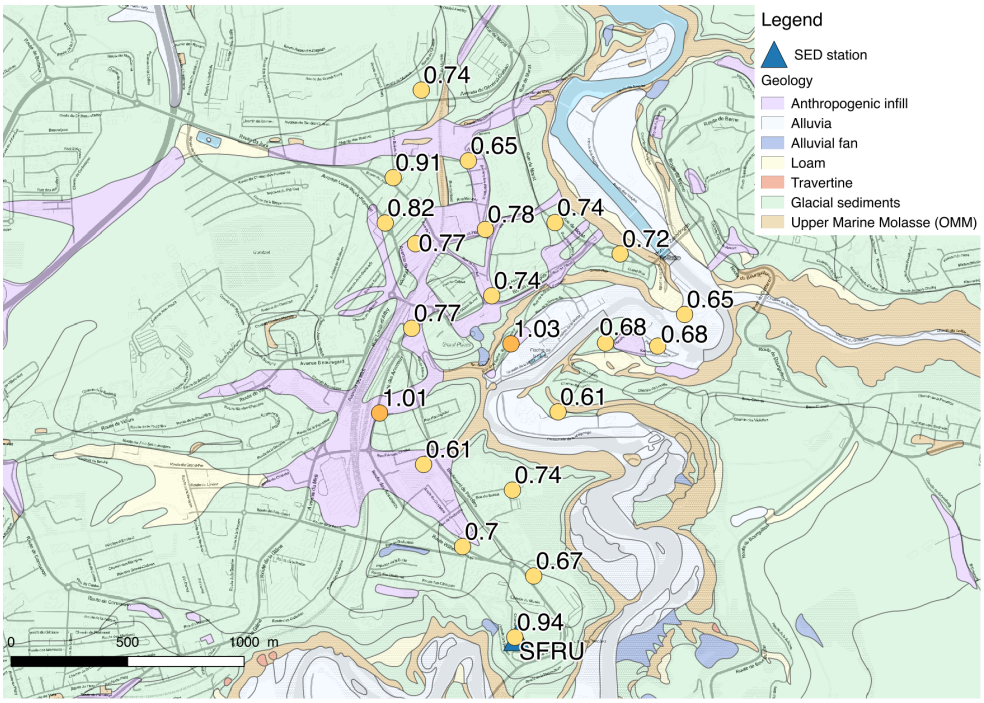

Figure 6: Map of the identified fundamental peaks in the H/V ratios (frequency values in Hz) for the whole city superimposed on the simplified geological map of the area (see Fig. 2 for the legend).

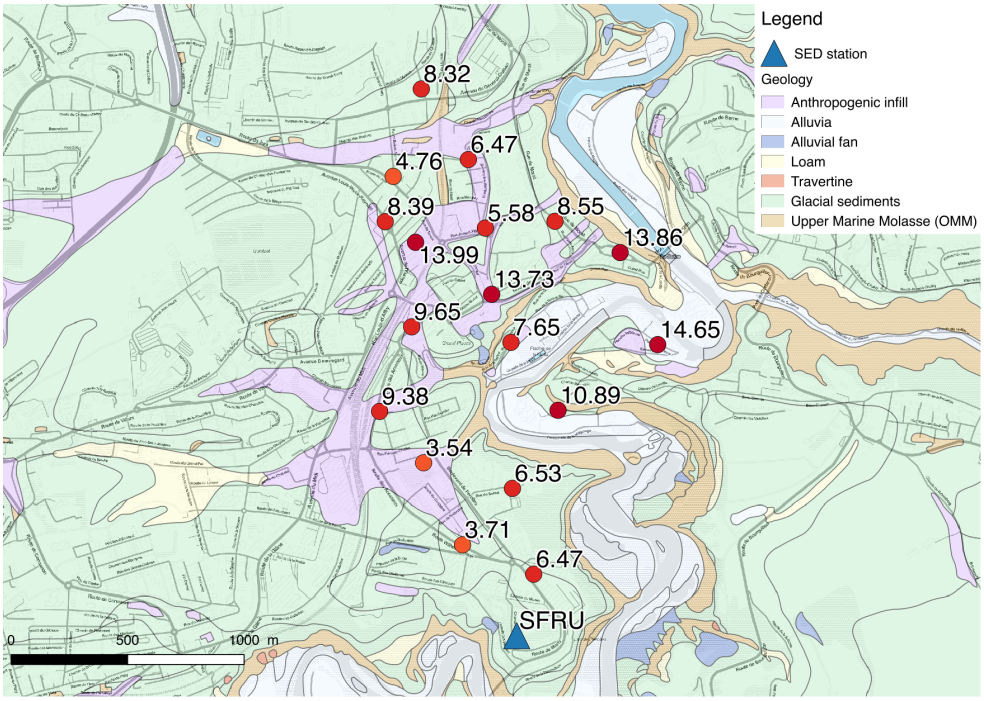

Figure 7: Map of the identified second peaks in the H/V ratios (frequency values in Hz) for the whole city superimposed on the simplified geological map of the area (see Fig. 2 for the legend).

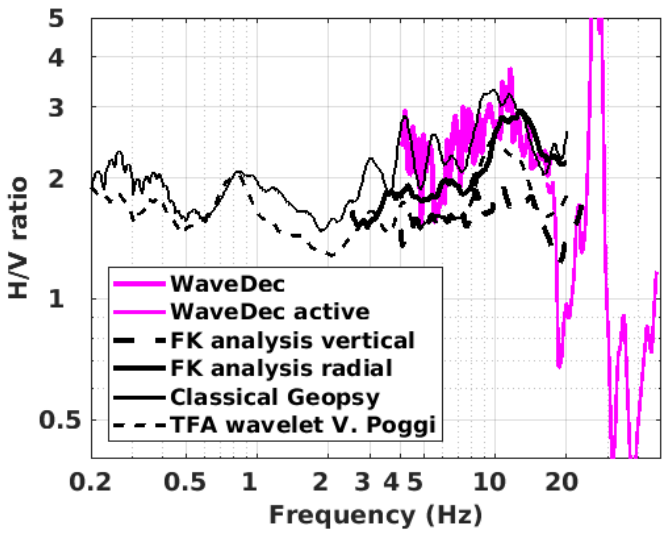

Figure 8: H/V spectral ratios for point FRU000 using the different codes. Classical methods were divided by $\sqrt{2}$.

3.2.2 Polarization analysis

Polarization analysis on the array data was performed to check for 2D resonance using the method of Burjánek et al. (2010). The wavefield does not show any particularly elliptical motion (Fig. 9). Therefore, 2D resonance can be excluded at this site.

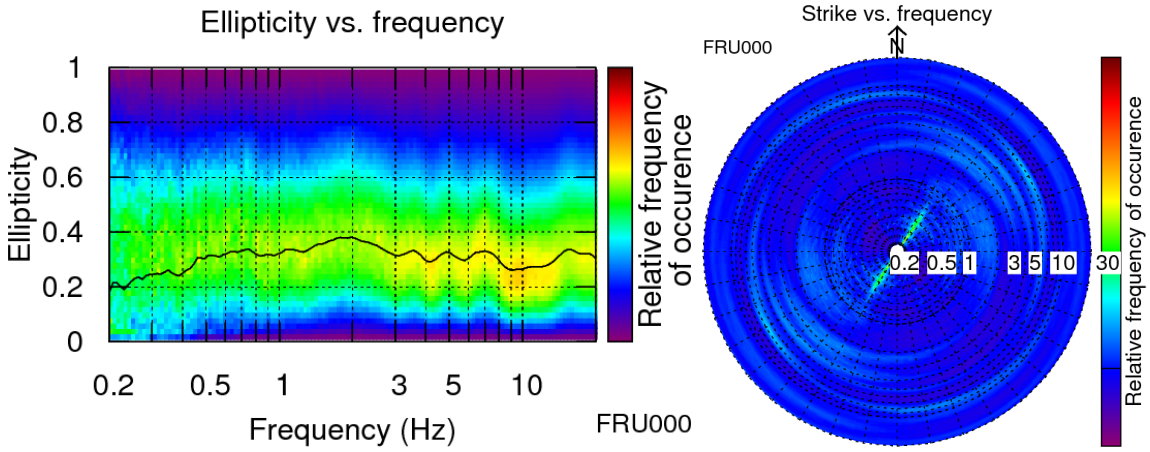

Figure 9: Polarization analysis at point FRU000. Left: Ellipticity (A trough in the ellipticity corresponds to polarized motion). Right: Strike of the polarization.

3.3 1- and 3-component high-resolution FK

In order to avoid biases due to lateral variations, both the full array and a sub-array excluding the largest ring have been processed. Fig. 10 shows the results of the 1C HRFK analysis of the whole array using Geopsy software. It shows a clear fundamental mode of Rayleigh waves between 4 and 18 Hz. The array was too small to capture lower frequencies. It can be noticed that curves are relatively flat (no strong increase of velocity, meaning that the only limitation was the array size, limited by the topography. This confirms the absence of strong velocity contrast, as also noted from the H/V analysis.This curve is bumpy with peaks at 4.75, 6 and 7.5 Hz, possibly due to harmonic disturbances or soil structure interaction. The results of the 3-component high-resolution FK analysis (Poggi and Fäh, 2010) are shown in Fig. 11 for the whole array. Rayleigh waves fundamental mode is also picked from the vertical direction in the same frequency band as for the 1C analysis but is not bumpy (though more uncertain). It does not match the results in the radial direction that lay between the fundamental Rayleigh and Love mode. The Love fundamental mode is clearly picked from 4 to 13 Hz. It has still energy at higher frequencies but the picking is disturbed by a strong aliasing due to the array geometry. The results for the sub-array are presented in Fig. 12. The resolution limit allows to retrieve curves only above 9-10 Hz. The difference with the whole array is not critical and is detailed in section 5.1.

The ellipticity curve determined with the 3-component HRFK analysis from the maxima picked on the vertical component is relatively flat and hardly matches the H/V ratios, while the one obtained using the maxima picked on the radial component matches well (see section 3.2.1 and Fig. 8). The results from the whole array and the sub-array are not noticeably different.

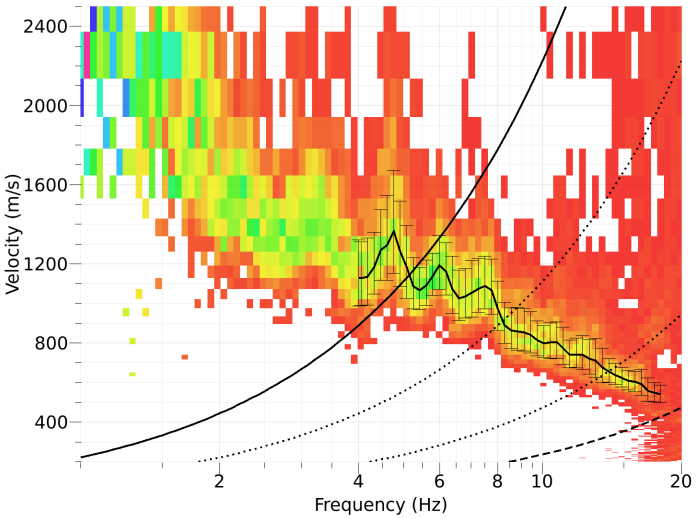

Figure 10: Dispersion curves obtained from the 1C HRFK analysis of the whole array.

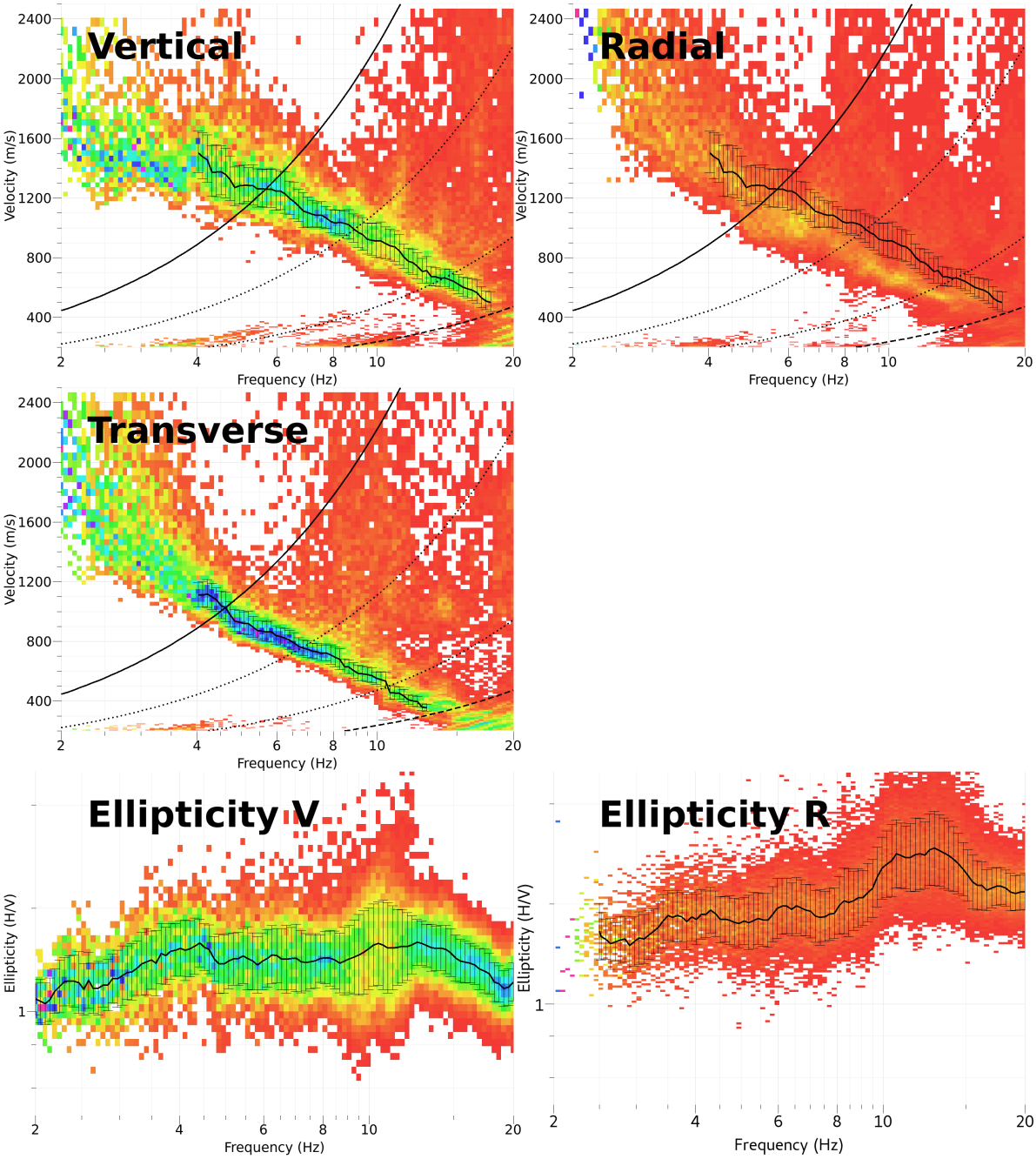

Figure 11: Dispersion curves obtained from the 3C HRFK analysis of the whole array.

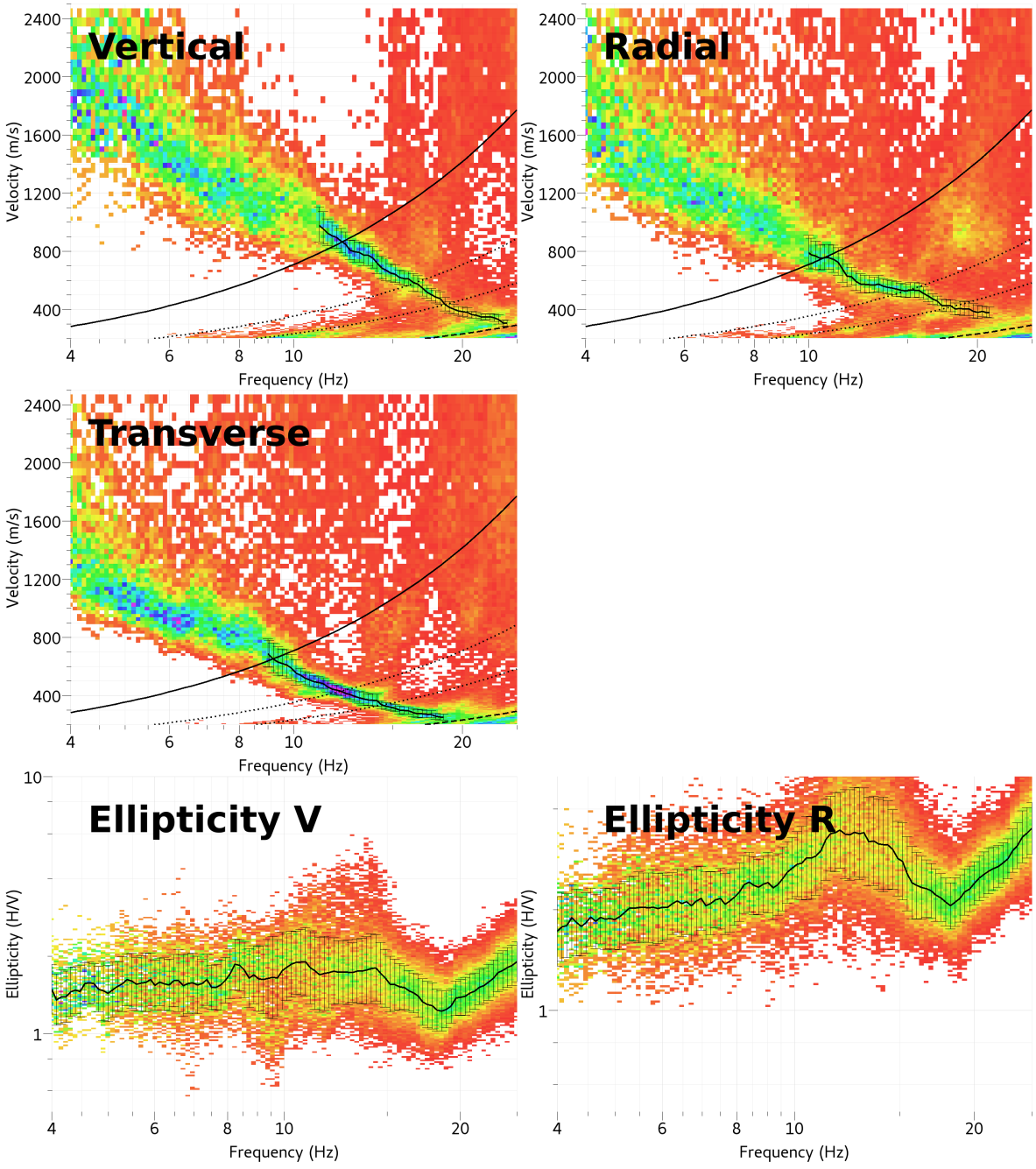

Figure 12: Dispersion curves obtained from the 3C HRFK analysis of the sub-array.

3.4 Wavedec

WaveDec (Maranò et al., 2012) has also been used to process the array data. This technique estimates the properties of multiple waves simultaneously with a maximum likelihood approach in the time domain. It was applied assuming the presence of 3 waves.
The fundamental Love and Rayleigh waves dispersion curves could be picked (Fig. 13) and are compared to the FK analysis in section 5.1. The ellipticity of Rayleigh waves (Fig. 14) is clear always retrograde in the investigated frequency band (4-17 Hz). The comparison with other proxys for the ellipticity curve is successfully performed in Fig. 8.

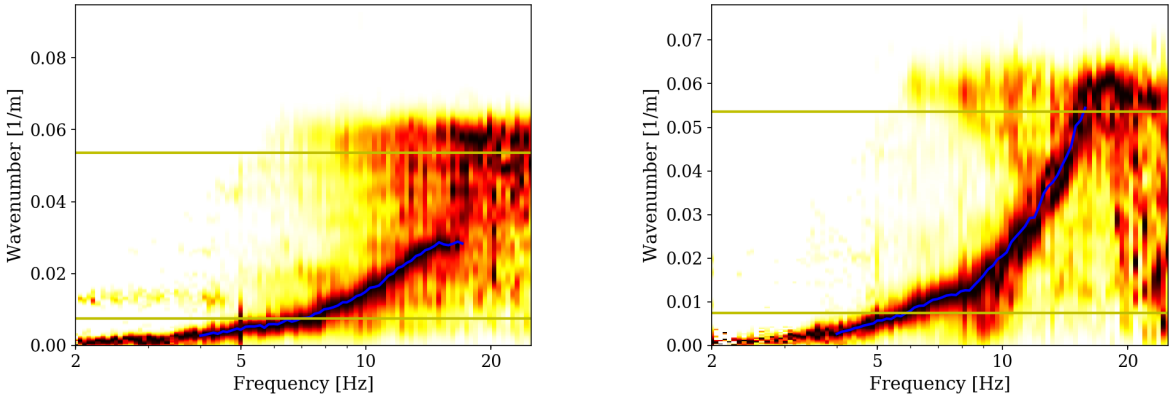

Figure 13: Rayleigh (left) and Love (right) waves dispersion curves obtained with the WaveDec technique (Maranò et al., 2012). The yellow lines indicate the theoretical array resolution limits.

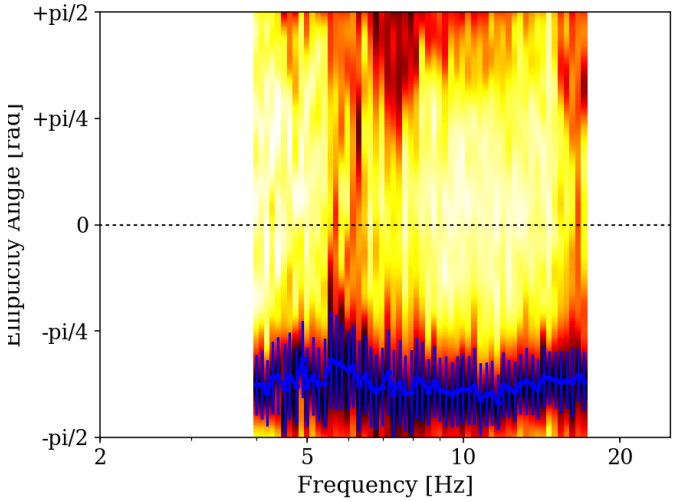

Figure 14: Rayleigh waves ellipticity curve obtained with the WaveDec technique (Maranò et al., 2012).

4 Site characterization using active measurements

At the targeted station (SFRU), an active seismic survey, besides passive measurements, was carried out. The purpose was providing seismic characterization of the shallow subsurface in close proximity with the SFRU station within a depth range (0-20 m depth) that is poorly investigated by, or out of reach of, noise recording techniques. Thanks to the use of controlled sources in proximity to the recording array, active measurements are meant to ensure signal coverage within a frequency band of approx. 10 - 70 Hz. For the sake of a comprehensive subsurface seismic characterization, both multichannel analysis of surface waves (MASW; Park et al., 1999) and P-wave refraction (Redpath, 1973) surveys were conducted.

4.1 Equipment

We used three sets of eight three-component geophones (4.5 Hz corner frequency). Each geophone set was connected to a Geode datalogger; the three Geodes were then coupled for time synchronization. The seismic source was 5 kg sledgehammer hitting a flat metal plate. Along the handle of the hammer, a trigger sensor was firmly fastened (and then connected to the Geodes) to ensure a convenient start of the acquisition window.

4.2 Geometry of the acquisition array

The acquisition spread was deployed along a forest path close to the SFRU station, approximately oriented from west to east (Fig. 15). The 24 geophones (see previous section) were arranged in a linear array and spaced by 2.1 m intervals (total length of the receiver line = 48.3 m). Most of the receivers were firmly coupled to the ground thanks to metal spikes attached to the base of the geophones; only the two westernmost geophones, located on the edge of an asphalt street running in north-south direction, were simply laid on the tarmac surface (Fig. 15). Five shot points were placed along the receivers spread: i) two at both ends of the geophones array, for the purposes of MASW acquisitions (src1 and src5 in (Fig. 15); ii) three more at 1/4, half, and 3/4 of the spread length (src2, src3 and src4, respectively): these shooting positions, together with those at the extremities of the array, were exploited for P-wave refraction acquisitions.

4.3 Acquisition

For both MASW and P-wave refraction acquisitions, seismic data were acquired using a sampling interval of 62.5 μs. The window length was set to 1 s (corresponding to 16000 samples) and a pre-trigger delay of -0.05 s was employed. At each source point, 10 hammer blows were successively shot; at each shot, the recordings from all geophones were saved in a separate .sg2 file. In Fig. 16, the seismic traces (vertical component) acquired having placed the source at the two extremities of the array, are displayed. Data quality appears to be relatively good, the useful seismic events (Rayleigh waves and P-wave first break arrivals) being clearly recognizable in the seismic sections. In Fig. 16, in the bottom panel, the surface wave train (labelled SW) and P-wave first break arrivals (labelled P) are highlighted. Unfortunately, few geophones belonging to the first set of receivers (0<X<14.7 m) had some malfunctioning components (as evident in Fig. 16); the corresponding traces were muted in the subsequent processing steps.

Figure 15: Map representing the location of the active seismic array and of the station SFRU (top: image produced with Google Earth) and picture of the deployment of the seismic array (bottom).

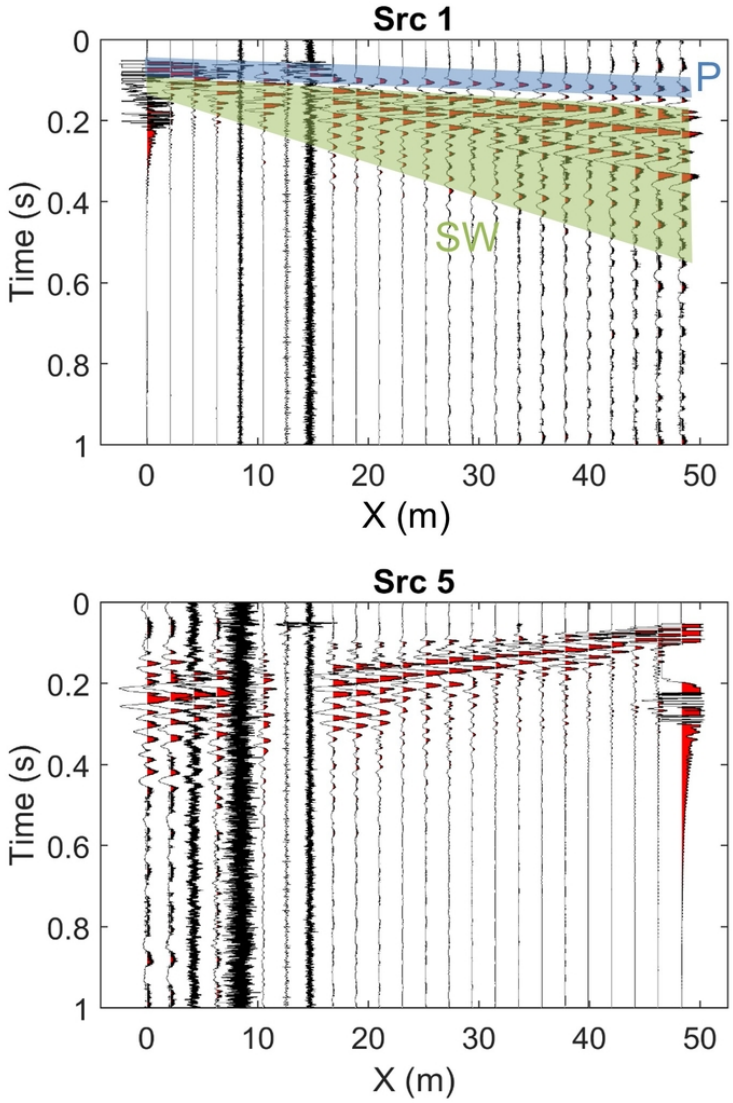

Figure 16: Seismic traces (vertical component) recorded by the geophones spread, having placed the seismic source at the western (src1, top) and eastern (src5, bottom), extremity of the recording spread. In the top panel, the P-wave first-break arrivals (P) and the surface wave train (SW) are highlighted. The X coordinate used in this representation is longitudinal to the geophone line, and it is oriented from the westernmost (X=0) to the easternmost (X=48.3 m) receiver. The same coordinate system will be used further in the text.

4.4 Processing

4.4.1 Pre-processing

Seismic traces generated by different shots, the seismic source being positioned at the same location, were summed - or stacked - in time domain. The scope of this operation is enhancing the coherent seismic events generated by the controlled seismic source (sledgehammer blow), and at the same time minimizing the incoherent noise anyhow present in the recordings (Foti et al., 2015). "Stacked" seismic sections, with greater signal-to-noise ratio, were hence obtained (Fig. 17). Comparing Fig. 17 with Fig. 16, it is evident the improvement in terms of signal-to-noise ratio (which improves as the square root of the number of repeated acquisitions, Foti et al., 2015), particularly at the long-offset traces.

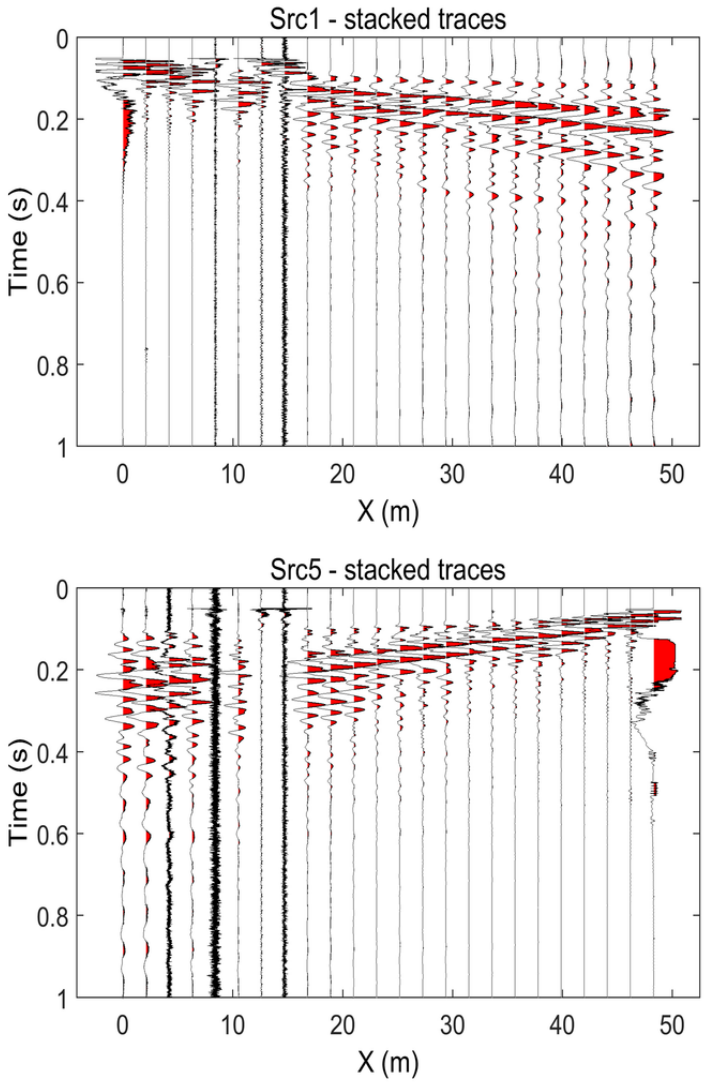

Figure 17: Stacked seismic sections (vertical component) obtained by summing the 10 different seismograms acquired positioning the seismic source at the western (src1, top) and eastern (src5, bottom) extremity of the recording spread (same of Fig. 16).

4.4.2 P-wave refraction processing

P-wave first break arrival times were manually picked on the stacked seismograms representing the vertical component of soil surface vibration (see Fig. 18, left panel). As anticipated in section 4.2, all five recording configurations were considered for P-wave refraction, the seismic source being positioned at both ends of the geophone array and at three intermediate locations. Fig. 18, right panel, displays all the picked travel time curves, or hodocrones. These appear to have a good reciprocal consistency (thus indicating a 1D geometry for the subsurface), with the exception of the arrivals at long offset, that show some lateral variability. This feature may suggest an irregular geometry for the deepermost interface illuminated by P-wave first-break arrivals; at the same time, this variability could be also attributed to the larger uncertainty range affecting long-offset picks.

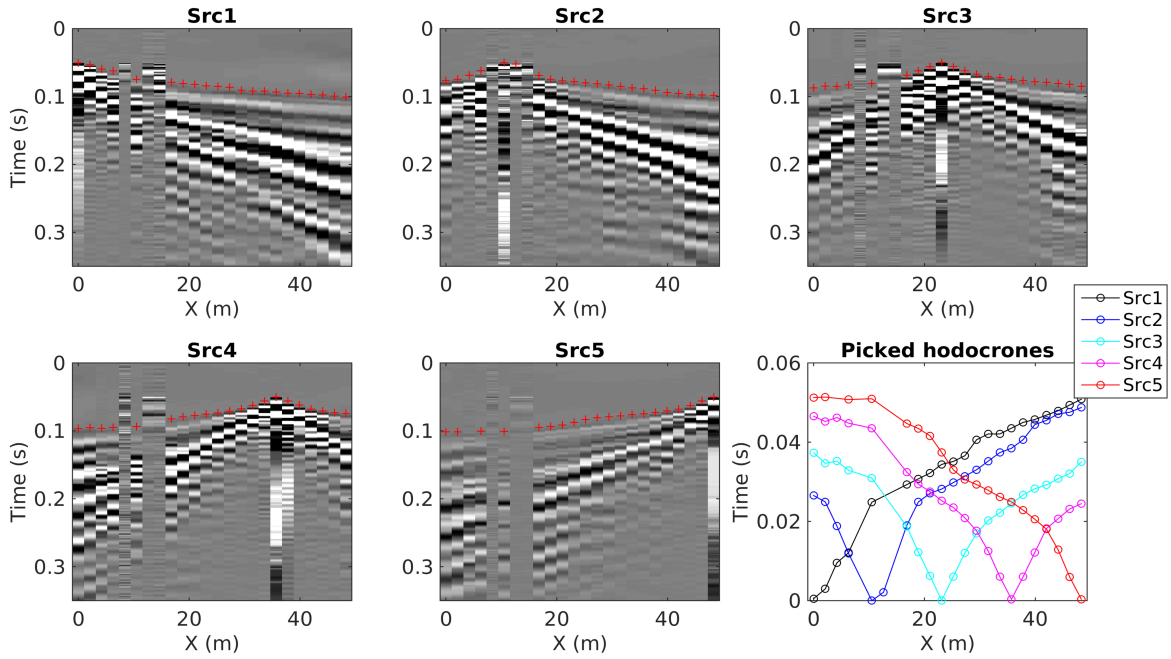

Figure 18: Top row panels and left and central panels from bottom row: picking of P-wave first break arrival times (red crosses) on vertical component seismograms obtained after the stacking of raw traces . Bottom-right panel: picked hodocrones from all available recording configurations. The X coordinate reference system is the same as Fig. 16, Fig. 17.

4.4.3 MASW processing

Vertical and longitudinal component seismograms from MASW acquisitions (src1 and src5), considering only single shot seismic sections, were processed by means of a 2D f-k (frequency-wavenumber) transform (Socco and Strobbia, 2004), so to obtain a conversion of the recorded sets of traces from time - offset to frequency - wavenumber domain. Before applying the f-k transform, short-offset traces (offset<6.3 m) were discarded, to avoid near-offset effects (Socco and Strobbia, 2004). The energy maxima in the retrieved f-k panels correspond to the propagation of Rayleigh waves and they depict the Rayleigh waves dispersive behavior (Socco and Strobbia, 2004; Foti et al., 2015). f-k images

belonging to the same acquiring configurations and referring to the same component (vertical or longitudinal) were stacked in the frequency-wavenumber domain to improve the signal-to-noise ratio. The picking of energy maxima was then carried out on such stacked f-k panels; the picking was first performed manually, defining regions of interest in the f-k domain, and then automatically identifying the peaks, frequency by frequency, within the selected areas (see Fig. 19a). The selected sets of maxima represent the extracted dispersion curves. The regions of interest manually defined during the picking operation were also automatically applied to the appropriate f-k spectra from single-shot seismograms. The obtained values are used to estimate the uncertainty intervals for the main dispersion curves, i.e. those derived from the stacked f-k images. Fig. 19b displays the resulting four dispersion curves (from shot positions src1 and src5, and from vertical and longitudinal component) and their uncertainties, in a phase velocity vs frequency representation. The extracted dispersive branches align relatively well along three main modes, that were identified as fundamental (extending within 10-70 Hz), first (20-80 Hz) and second higher mode (40-60 Hz). Nevertheless, the mode attribution for the low-frequency points (<13 Hz for the fundamental mode, <20 Hz for the first higher mode) is somehow not certain , as mode jumps might be present (also as suggested by subsequent processing steps, see later in the text). Lastly, the obtained four curves were merged – through averaging - into a single, final dispersion curve (Fig. 19c).

4.5 P-wave refraction interpretation

P-wave refraction data (section 4.4.2) were interpreted with the method of intercept time analysis (Reynolds, 2011). Following the hypothesis of a 1D geometry for the shallow subsurface (sections 4.4.2), the hodocrones obtained from refraction processing were collapsed in a single travel-time curve in time-offset domain (black circles in Fig. 20a). The obtained travel-time curve appears to be divided into three portions, with decreasing slope: one extending at offsets < 8 m, with steeper slope, and interpreted as the segment of direct arrivals; the second and third part of the hodocrone ($8 < offset < 27$ m and $offset > 27$ m) , collect the arrival times refracted along the interface 1st-2nd layer and 2nd-3rd layer, respectively. Applying the intercept time equations, the obtained VP profile is hence a three-layer model, with a surficial layer having VP = 362 m/s and thickness = 2.7 m, overlying an intermediate formation with VP = 1057 m/s and 10.1 m, thick , in turn resting on a halfspace having VP=2570 m/s (Fig. 20b). To assess the reliability of the estimation of each parameter, we performed a sensitivity analysis over the obtained model, perturbing each parameter in a $\pm$35% interval, and then evaluating the resulting change in the fit of the data. The results of the sensitivity analysis are displayed in Fig. 20c. Each row corresponds to a model parameter, either velocity (VP) or thickness (H); the abscissae refer to the parameter perturbation, while the color scale represents the corresponding relative change in the data fit, expressed as RMS error. In each row, the black lines span the perturbation interval bounded by a $+$2.5% relative change of the RMS error. It is possible to conclude that the parameters related to the shallowest portion of the subsurface (VP1,VP2,H1) are fairly constrained by the data; on the other hand, the interface between 2nd and 3rd layer and the velocity of the halfspace have extremely wide uncertainty intervals.

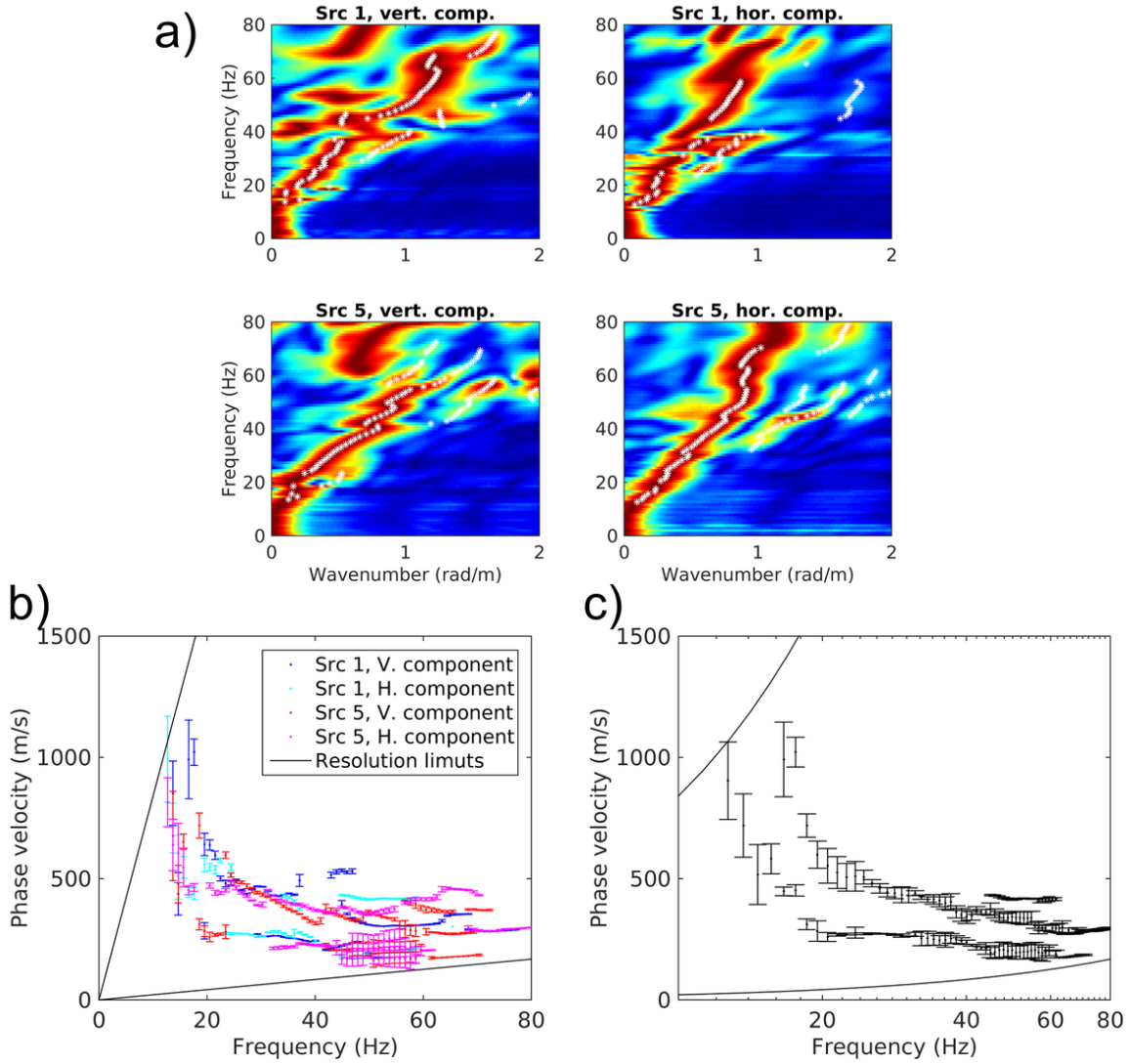

Figure 19: a) Normalized stacked f-k spectra obtained from vertical and longitudinal component recordings from MASW configurations of acquisition; picked maxima are represented as white asterisks. b) the corresponding four dispersion curves; c) the final dispersion curve obtained averaging the curves in (a).

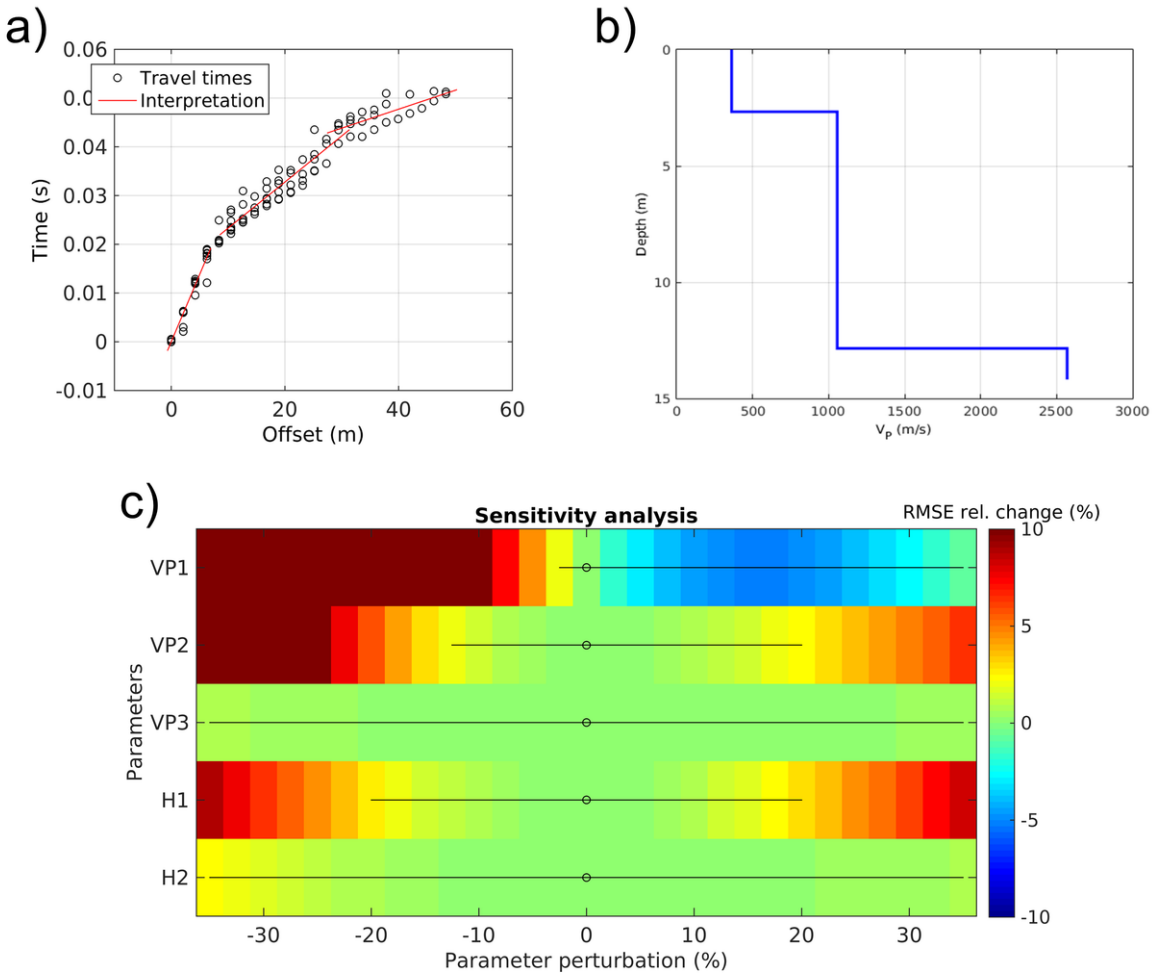

Figure 20: P-wave travel time interpretation. a) travel time data points (black circles) and linear fitting of the three hodocrone segments (red lines). b) Obtained surficial P-wave velocity model. c) sensitivity analysis performed over the obtained VP model. Each row corresponds to a model parameter, either velocity (VP) or thickness (H); the abscissae refer to the parameter perturbation, while the color scale represents the corresponding relative change in the data fit, expressed as RMS error.

4.6 WaveDec active

For completeness of analysis, the seismic traces generated with the use of the sledgehammer and recorded by the passive array, were also processed with the use of the software WaveDecActive (Maranò et al., 2017). This programme is an adaptation of WaveDec code (Maranò et al., 2012), initially conceived for the processing of noise recordings, to active surface wave acquisitions. It performs a maximum likelihood estimation of surface wave propagation parameters, jointly modeling all recorded components of the recorded velocity field (vertical, radial, transversal). The criterion for the identification of the type (Rayleigh, Love) and number of waves "contained" in the measured data is a penalized version of the Bayesian information criterion (BIC), with a scalar γ balancing between a purely BIC ($\gamma = 0$) or a maximum likelihood approach ($\gamma = 1$). We processed with WaveDecActive all seismic sections acquired having positioned the seismic source at scr1 and src5; faulty traces were discarded from the analysis. In Fig. 21a,b we represent the estimated Rayleigh wave propagation parameters, i.e. phase velocities (Fig. 21a) and ellipticity angles (Fig. 21b). In the phase velocity vs frequency panel (Fig. 21a), it is possible to identify a series of dispersive events that can be interpreted as modes of Rayleigh wave propagation; the three slowest events largely coincide with the fundamental, first and second higher mode resulting from the f-k analysis of the same data. The estimated ellipticities appear to have reasonable values for the data from src1, but not those from src5 (that assume values $= \pm 2\pi$). As already experienced in the processing of other datasets (e.g. site characterization at station SFEL), WaveDecActive (particularly in the estimation of the ellipticity) is extremely sensitive to the presence of traces with minor flaws (e.g. a geophone poorly coupled to the ground, or geophones placed on different surfaces), that lead the global result towards unreasonable outcomes. In Fig. 21c and Fig. 21d we represent exclusively the results obtained from src1 data, highlighting the phase velocity and ellipticity estimates for the fundamental and 1st higher mode of Rayleigh waves in cyan and magenta, respectively.

While using the sledgehammer source for active data acquisition (with the geophone array), the produced seismic signals are also recorded by the sensors from the passive array (see Fig. 22a for an example). Therefore, we isolated the time-windows from the continuous noise recordings "containing" the signal related to the use of the sledgehammer, and processed these traces too with WaveDecActive. The goal is twofold: i) testing the applicability of a combined use of the passive array in passive and active surface wave measurements, as suggested by Maranò et al. (2017); ii) extending the analyzed wavelength range towards longer wavelengths, as allowed by the larger extent of the passive array. Firstly, we conducted some tests to determine the offset range to be included in the analyses (Fig. 22a). Short-offset traces (<10 m) are to be excluded, because of evident "tilting" effects; on the other hand, beyond a certain offset (determined to be 67 m) the signal generated with the hammer is too corrupted. Nevertheless, the selected offset range (10 – 67 m) ensures a good azimuthal coverage (Fig. 22b)and it includes most of the acquired traces (Fig. 22c).
As the obtained results soon appeared to be unclear and rich in outliers (Fig. 23a,b), we performed multiple processing attempts assuming increasing values for the γ parameter (see earlier in this section), and testing different maximum number of waves to be identified in the data. For the sake of brevity, we show here only the most successful results, having selected a maximum number of 5 waves and $\gamma = 0.3$ (Fig. 23a,c)

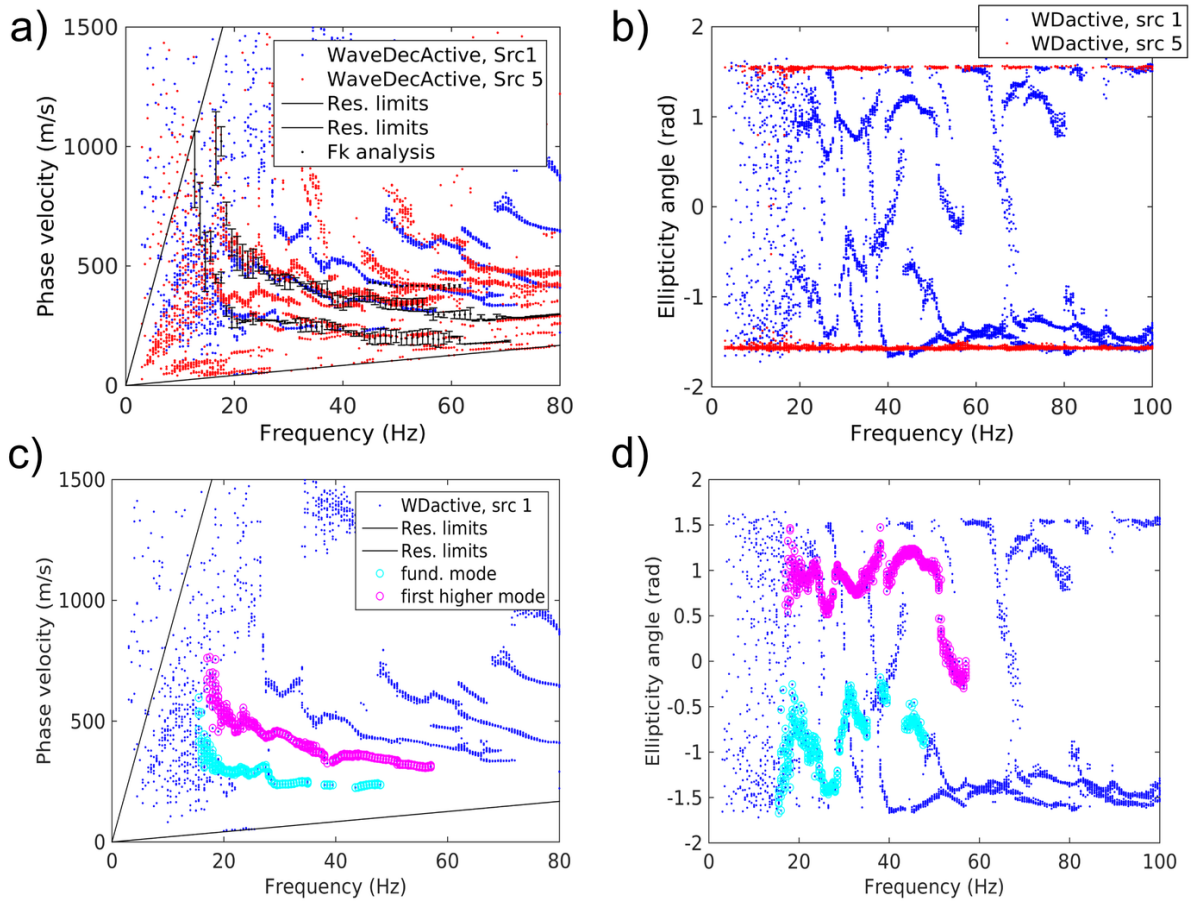

Figure 21: MASW data processing with WaveDecActive. a) estimated Rayleigh wave phase velocities, from seismic traces acquired with the seismic source positioned in src1 (blue dots) or src5 (red dots). These are collated with the dispersion curve from f-k processing (black dots). b) Estimated Rayleigh wave ellipticity angles, from seismic traces acquired with the seismic source positioned in src1 (blue dots) or src5 (red dots). c) estimated Rayleigh wave phase velocities, from seismic traces acquired with the seismic source positioned in src1 (blue dots); the data points recognized as belonging to the fundamental and 1st higher mode are highlighted with cyan and magenta circles, respectively. d) Same as (c), although referred to ellipticity angles.

and $\gamma = 0.5$ (Fig. 23b,d). Choosing a higher value for γ decreases indeed the number of outliers, but also the number of "meaningful" data points (compare Fig. 23a,c with Fig. 23b,d). Some identified phase velocities estimates define patterns (in the 15 to 50 Hz frequency band) close enough to the fundamental and 1st higher mode as obtained from the geophone data processing (see Fig. 23c,d). Also, around 12-13 Hz and 600 m/s the identified fundamental and 1st higher mode appear to draw an osculation point, that has probably compromised the mode numbering at low frequency of the f-k analysis results (4.4.3). Beyond that, unfortunately, it is not possible to obtain reliable results at lower frequencies, as it was originally intended.

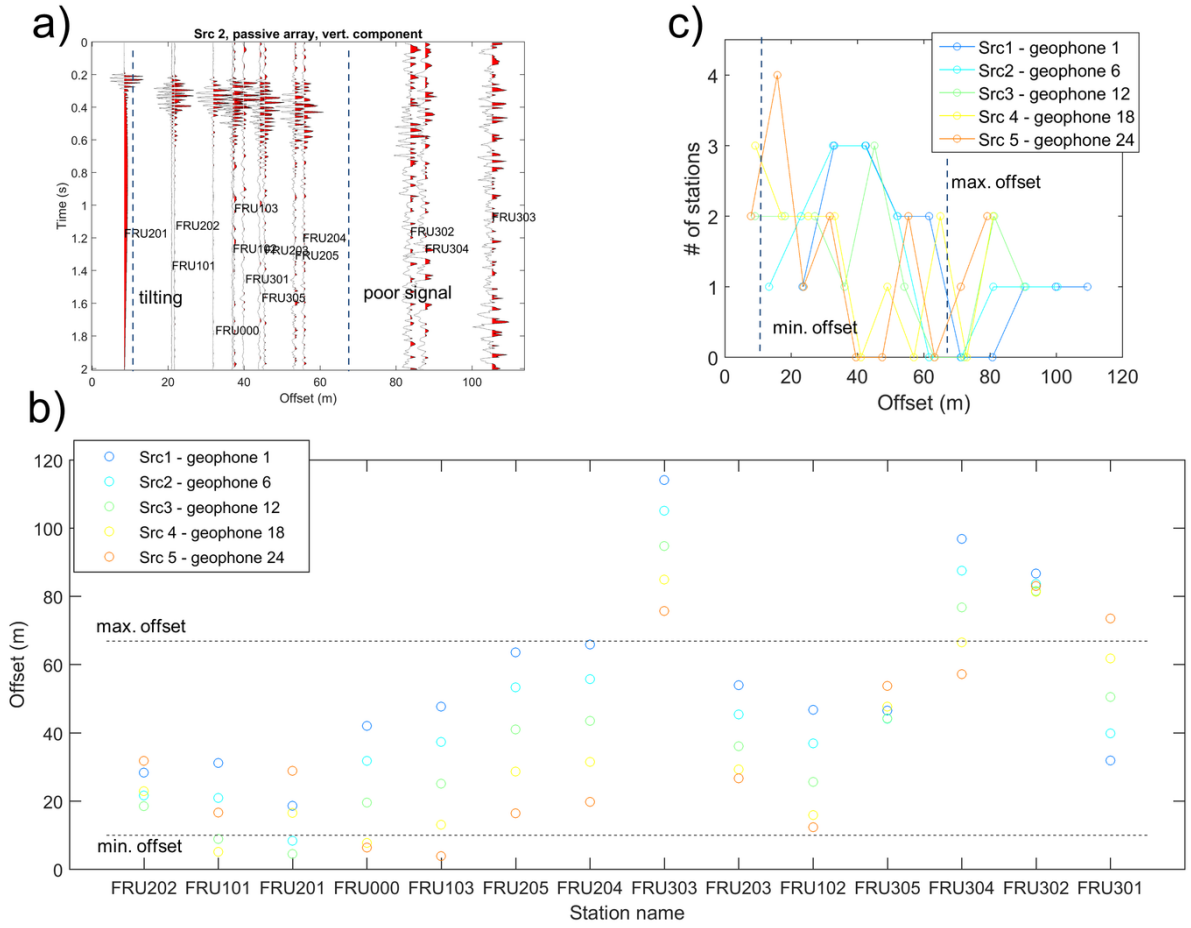

Figure 22: Active data acquired with passive array. a) seismic sections collecting the traces (vertical component) recorded by passive array sensors, the source being positioned at src2. b) Source-to-receiver offset for all passive array sensors, considering different sources positions (src1-5). c) Histograms representing the source-to-receiver offset distribution considering different sources positions (src1-5)

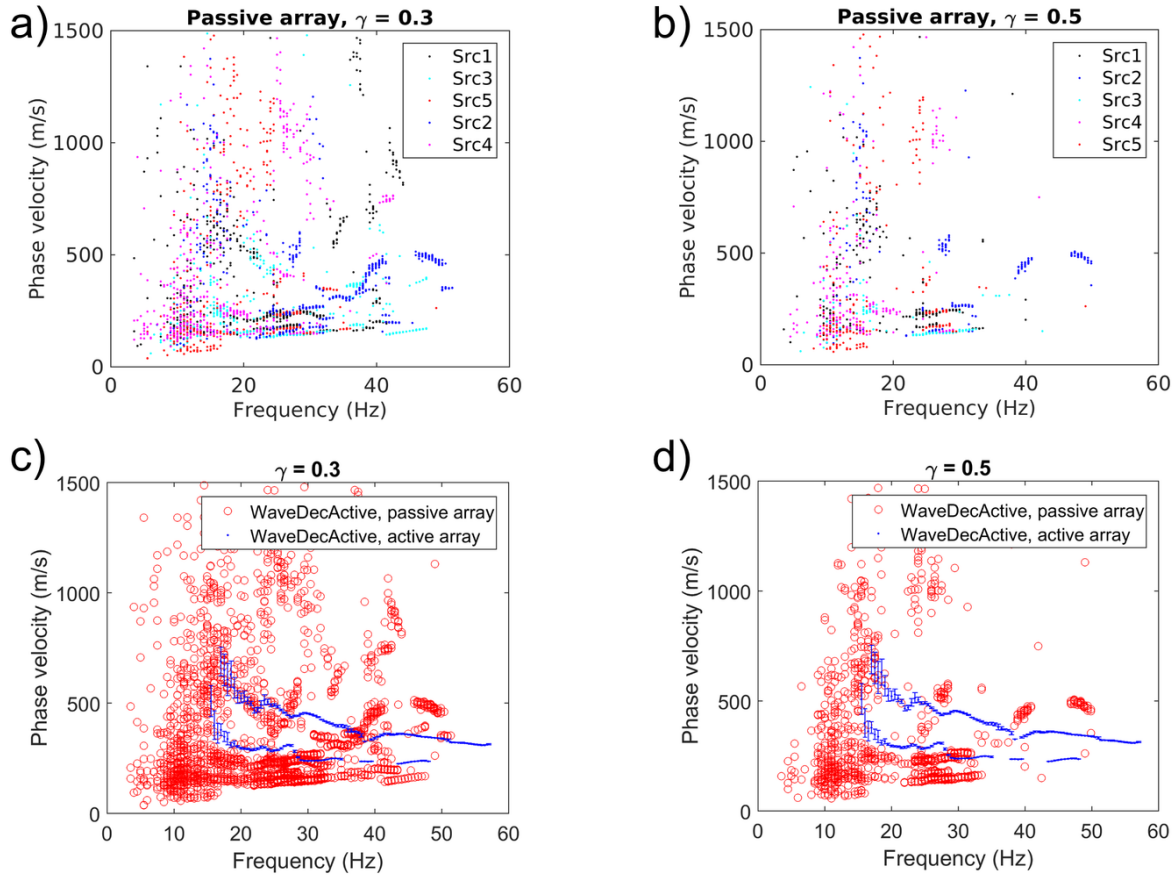

Figure 23: Active data acquired with passive array, processed with WaveDecActive. a) estimated phase velocities, having selected a γ value of 0.3 for the processing. Different colors refer to the corresponding source position. b) Same as (a), having selected a γ value of 0.5 for the processing. c) estimated phase velocities, having selected a γ value of 0.3 for the processing (red circles), superimposed to the dispersion curve obtained from geophone data. d) Same as (c), having selected a γ value of 0.5 for the processing

5 Interpretation of the surface wave properties and inversion

5.1 Interpretation of the dispersion curves

Fig. 24 gives an overview of the dispersion curves determined with the different methods and sub-arrays. The thin lines in Fig. 24 correspond to the processing of the two smallest rings only. Love fundamental dispersion curve, although small variations due to the lateral variations is consistently retrieved from 4 to 17 Hz. The biggest issue is the discrepancy between Rayleigh curve retrieved from WaveDec, corresponding to the dispersion obtained with the radial component of 3C FK and the curves obtained using the vertical component (3C and 1C FK). Although it is negligible at low frequency and it disappears at 20 Hz, It is noticeable between 6 and 20 Hz. The continuity with the high frequency curves from the active experiment is ensured in any case. Those are very consistent whatever the processing technique used (WaveDec or FK). It can be however noticed that due to the lateral variability of the few upper meters, the active results and passive processing using the sub-array show a shift at 15-25 Hz. Rayleigh dispersion curve is retrieved form 4 to 70 Hz.

For the inversion, the Rayleigh and Love fundamental modes have been selected based on all these results. For Rayleigh waves, the radial component has been trusted because it gave better results in the inversion. The selected curves are displayed in Fig. 25.

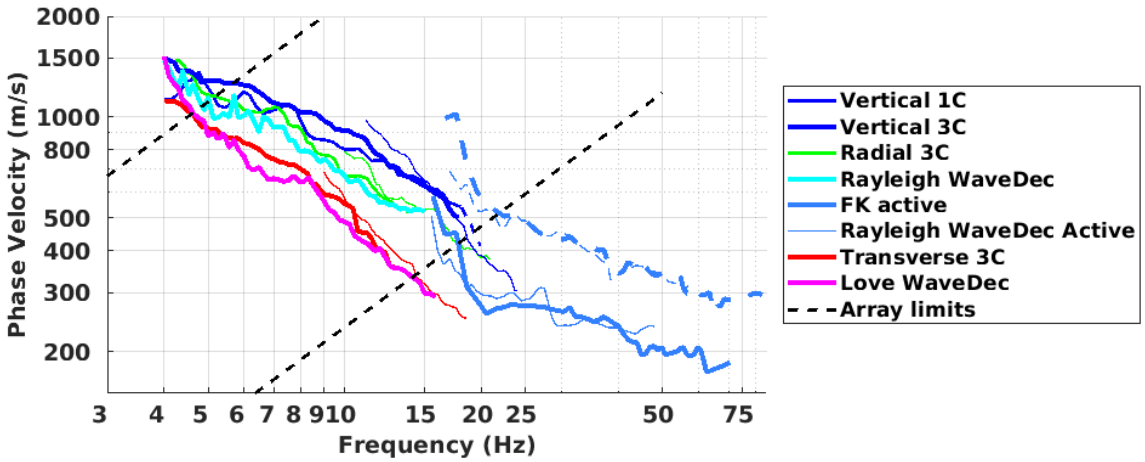

Figure 24: Picked dispersion curves from 1C and 3C HRFK analysis.

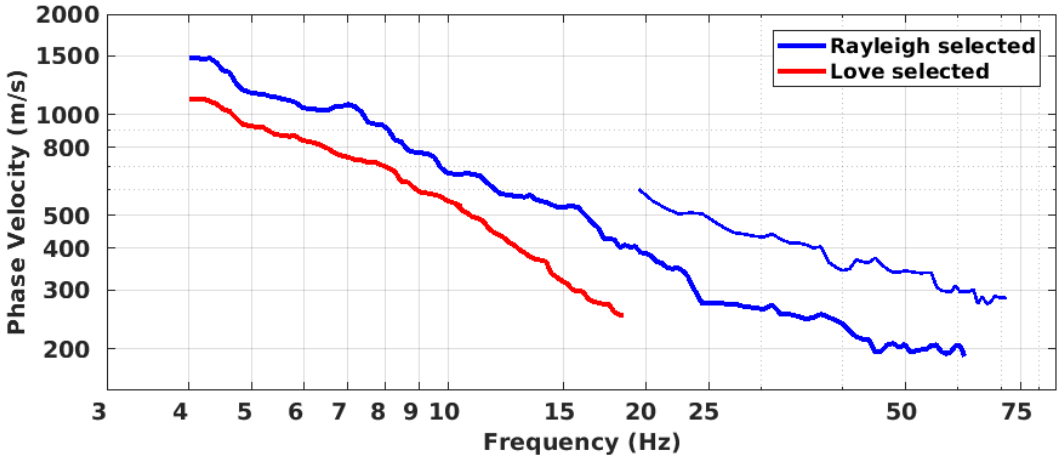

Figure 25: Selected dispersion curves for SFRU site.

5.2 Misfit functions

The inversion of the surface waves properties into 1D velocity profiles was performed using the Improved Neighborhood Algorithm (NA) (Wathelet, 2008) implemented in the Dinver software.
The misfit function is based on the selected Love and Rayleigh fundamental modes, the Rayleigh first higher mode and the ellipticity from the H/V curve computed with the TFA code of V. Poggi at point FRU000. The H/V curve is used with a weight of 0.2.
All curves were resampled using 50 points between 0.4 and 60 Hz in log scale. No uncertainty was considered in the misfit function (all points with the same weight).

5.3 Parametrization of the model space

To parametrize the model space, we assumed increasing velocity with depth and based the parametrization on the refraction results. The first layer was assumed to be about 2.7 m thickness with little uncertainty and the second layer 10.2 m with 35% uncertainty. Vp range in those layers was limited to 300-400 m/s and 600-1200 m/s, respectively. The Poisson ratio was inverted in the range 0.2-0.4. The density was assumed to be 2000 kg/m^3 in the sediments and 2500 kg/m^3 in the molasse bedrock. Inversions with free layer depths as well as fixed layer depths were performed. The velocity gradient in the rock requires a large number of layers to be well modelled. We performed 5 independent runs of 5 different parametrization schemes (5 and 6 free layers over a half space and 10, 11 and 11 layers with fixed depth over a half space) were performed, i.e. a total of 25 runs.

5.4 Results

Examples of retrieved ground profiles for the different misfit functions and parametrization strategies are presented in Fig. 26. When comparing to the target curves (Fig. 27 and Fig. 28), dispersion and ellipticity curves are well reproduced. The only deviation concerns Love waves above 13 Hz.
For further elaborations, the best models of these 25 runs were selected and used (see section 6.1).

6 Interpretation of the velocity profiles

6.1 Velocity profiles

The profiles have a first layer of unconsolidated sediments of about 2.5 m thickness (prescribed) with shear wave velocities of 200-225 m/s. Vp retrieved with the surface waves inversion tend to larger values than the refraction (362 m/s), but was limited to 400 m/s. The obtained results correspond to a Poisson ratio between 0.25 and 0.3. The interface with the stiffer sediments located below would correspond to a resonance frequency of about 20 Hz that was not investigated. The second layer reaches a depth of about 6 to 13 m (value from the refraction: 12.85 m/s) and is made of unconsolidated moraine sediments with shear wave velocities between 330 and 450 m/s. The Poisson ratio is about 0.35 in this part. Vp is between 650 and 1000 m/s, while the value from

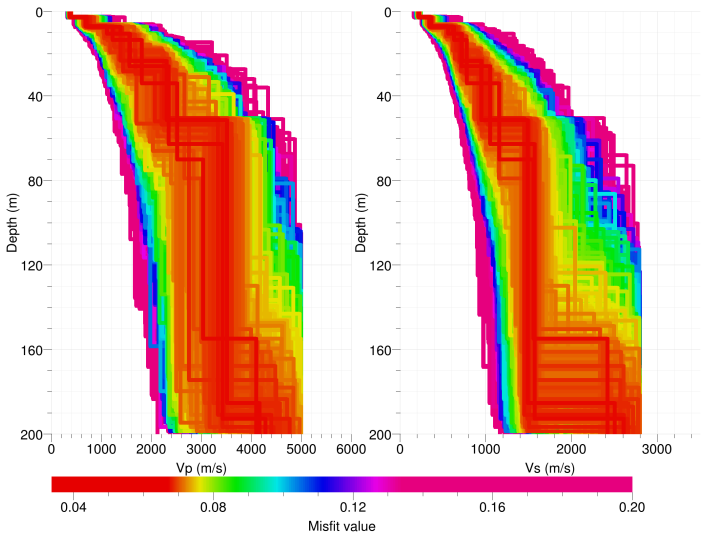

Figure 26: Inverted ground profiles at SFRU in terms of V_p and V_s using the free layer depth strategy.

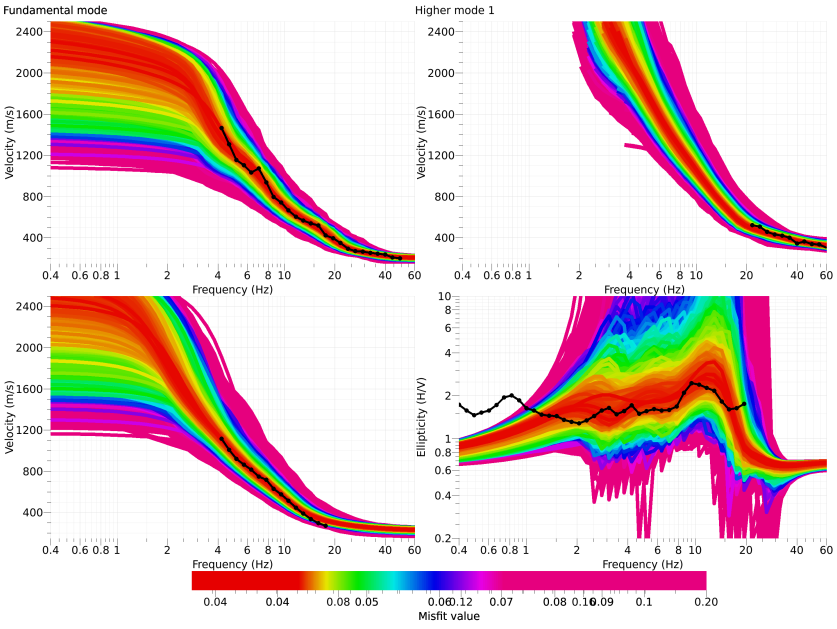

Figure 27: Comparison between inverted models and measured Rayleigh (top row: dispersion fundamental and first higher modes and bottom right: ellipticity) and Love (bottom row: left) waves at site SFRU using the free layer depth strategy.

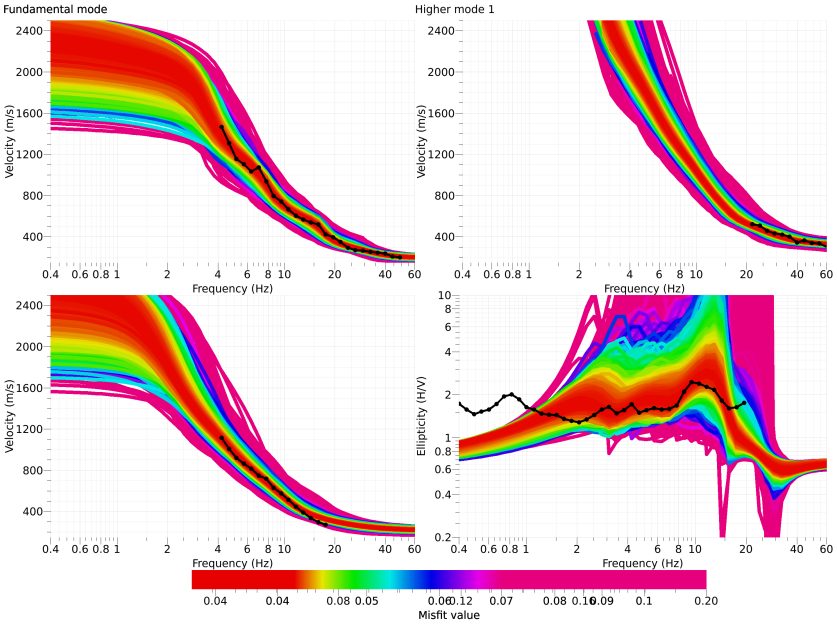

Figure 28: Comparison between inverted models and measured Rayleigh (top row: dispersion fundamental and first higher modes and bottom right: ellipticity) and Love (bottom row: left) waves at site SFRU using the fixed layer depth strategy.

the refraction is 1057 m/s. The interface with the underlying consolidated sediments is responsible for a resonance peak of about 10 Hz that was recognized in the H/V analysis. Those are moraine and fluvial-glacial sediments that can be found down to about 45 m depth ($\pm$15 m). This is in accordance with the geological profile in the Sarine gorges. It has a shear-wave velocity of about 750 m/s (680-970 m/s). The Vp value from the refraction is too large because it misses this intermediate layer of sediments. It should produce a peak in the H/V of about 3.7 Hz that is however too small to be seen. The underlying rock at this depth is made of Molasse with a shear wave velocity increasing from about 1330 m/s at 50 m up to about 1500 m/s at 100 m depth. The increase is going on below 150 m depth but not reliably retrieved.

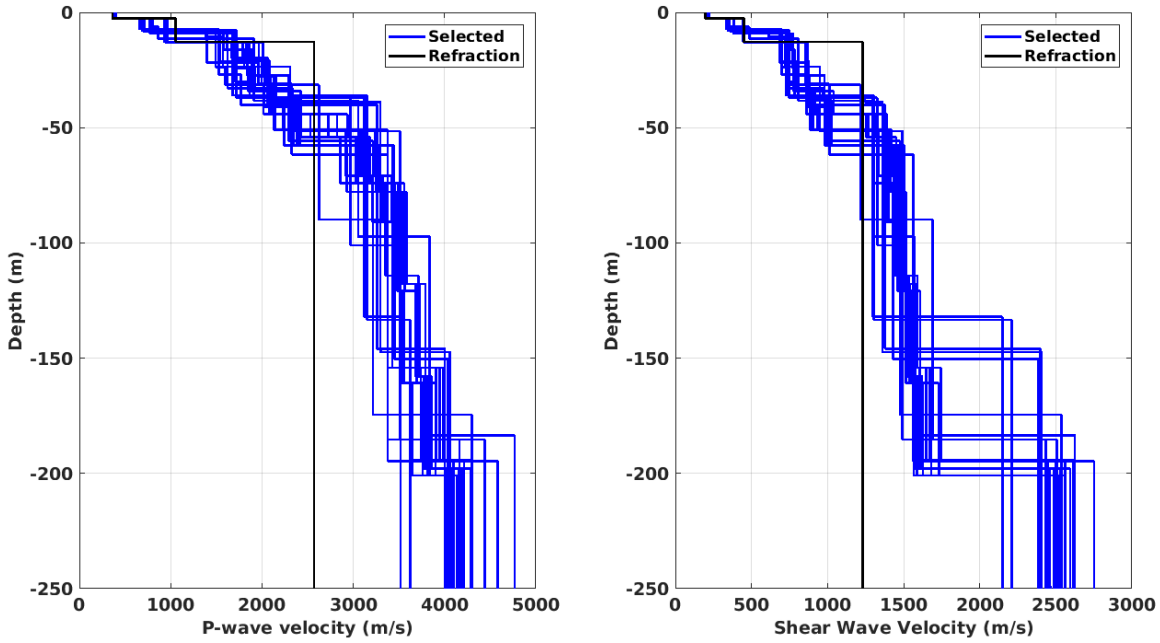

Figure 29: P- (left) and S- (right) waves velocity profiles of the 25 selected models. The blue color relates to the surface waves inversion and the black line to the results of the refraction (S-wave velocities are invented).

The distribution of the travel time average velocities at different depths was computed from the selected models. $V_{s,30}$ is found to be 534 m/s. These profiles correspond to ground type B in the Eurocode 8 (CEN, 2004) and in the SIA261 (SIA, 2014). They are not assigned to ground type E because the material below the major interface barely reaches 800 m/s (only few profiles) and can hardly be considered as the "bedrock". The velocity in the sediments is generally meeting the code criteria of type E, however. The old SIA269 ground type E did not require a strong bedrock (type A or B) which explains the deviation from the official map.

6.2 Quarter-wavelength representation

The quarter-wavelength velocity approach (Joyner et al., 1981) provides, for a given frequency, the average velocity at a depth corresponding to 1/4 of the wavelength of interest. It is useful to identify the frequency limits of the experimental data (minimum frequency in dispersion curves at 4 Hz). The results using this proxy show that the dispersion curves constrain the profiles down to 35 m (Fig. 30). Moreover, the quarter wavelength impedance-contrast introduced by Poggi et al. (2012a) is also displayed in the figure. It corresponds to the ratio between two quarter-wavelength average velocities, respectively from the top and the bottom part of the velocity profile, at a given frequency (Poggi et al., 2012a). It shows a trough (inverse shows a peak) at the resonance frequency.

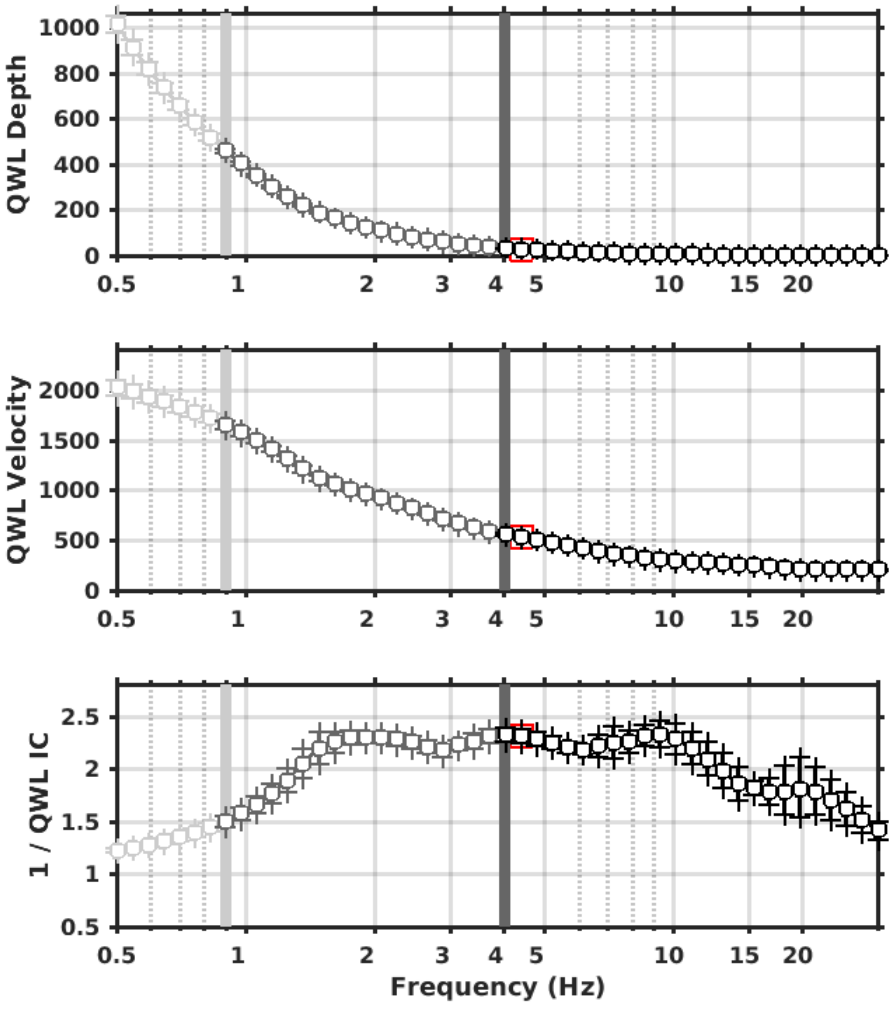

Figure 30: Quarter wavelength representation of the velocity profile for the selected velocity profiles (top: depth, center: velocity, bottom: inverse of the impedance contrast). The black curves are constrained by the dispersion curves, the grey curves are weakly constrained by the ellipticity curve and the light grey curves are not constrained by the data. The red square corresponds to V_{S30}.

6.3 SH transfer function

The theoretical SH-wave transfer function for vertical propagation (Roesset, 1970) is computed from the selected profiles. It is corrected with respect to the Swiss Reference Rock model (Poggi et al., 2011) following Edwards et al. (2013). It shows an increasing amplification with frequency with a peak around 10 Hz (amplification of a factor of 3.5) (Fig. 31). Interestingly, it shows a small peak around 5 Hz that could correspond to what was seen on the H/V curves.
It could not be compared to the amplification function obtained by empirical spectral modelling (ESM) (Edwards et al., 2013; Michel et al., 2014, 2017) at station SFRU since not enough recordings are available to date.

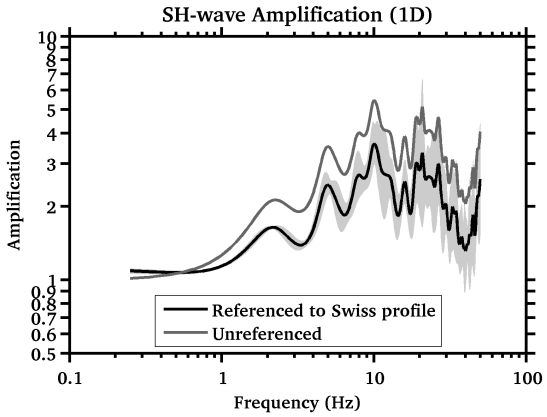

Figure 31: Amplification at site SFRU using the SH transfer function with respect to the local bedrock and to the Swiss reference rock model with its standard deviation.

7 Conclusions

The combined passive and active measurements presented in this study were successful in deriving a velocity model for the site SFRU. The profiles show three layers of morainic and infra-morainic sediments: 2.5 m at 200 m/s, about 8 m at 400 m/s and about 35 m at 750 m/s. Below these sediments, one finds Molasse rock with increasing velocity starting at 1300 m/s at 45 m depth. The clearest contrast occurs between the second and the third sediment layers, at about 10 m depth, corresponding to a peak at 10 Hz.
$V_{s,30}$ is 534 m/s and the site corresponds to ground type B in the Eurocode 8 (CEN, 2004) and the SIA261 (SIA, 2014). The theoretical 1D SH transfer function computed from the inverted profiles shows an increasing amplification with frequency with a peak at 10 Hz reaching an amplification of a factor of 3.5. While this site can be considered as representative for the city of Fribourg, strong lateral variations are expected. More recordings at the station SFRU are however needed to validate this site characterization using Empirical Spectral Modelling.

Acknowledgements

The authors thank David Farsky for his help with the measurements. An article written by T. Araman on this measurement was published in "Migros magazine" in June 2017.

References

Burjánek, J., Gassner-Stamm, G., Poggi, V., Moore, J. R., and Fäh, D. (2010). Ambient vibration analysis of an unstable mountain slope. *Geophysical Journal International*, 180(2):820–828.

CEN (2004). *Eurocode 8: Design of structures for earthquake resistance - Part 1: General rules, seismic actions and rules for buildings*. European Committee for Standardization, en 1998-1: edition.

Edwards, B., Michel, C., Poggi, V., and Fäh, D. (2013). Determination of Site Amplification from Regional Seismicity : Application to the Swiss National Seismic Networks. *Seismological Research Letters*, 84(4).

Fäh, D., Kind, F., and Giardini, D. (2001). A theoretical investigation of average H/V ratios. *Geophysical Journal International*, 145(2):535–549.

Foti, S., Lai, C. G., Rix, G. J., and Strobbia, C. (2015). *Surface Wave Methods for Near-Surface Site Characterization*. CRC Press, Taylor & Francis Group LLC.

Joyner, W. B., Warrick, R. E., and Fumal, T. E. (1981). The effect of Quaternary alluvium on strong ground motion in the Coyote Lake, California, earthquake of 1979. *Bulletin of the Seismological Society of America*, 71(4):1333–1349.

Maranò, S., Hobiger, M., Bergamo, P., and Fäh, D. (2017). Analysis of Rayleigh waves with circular wavefront: a maximum likelihood approach. *Geophysical Journal International*, 210(3):1570–1580.

Maranò, S., Reller, C., Loeliger, H. A., and Fäh, D. (2012). Seismic waves estimation and wavefield decomposition: Application to ambient vibrations. *Geophysical Journal International*, 191(1):175–188.

Michel, C., Edwards, B., Poggi, V., Burjánek, J., Roten, D., Cauzzi, C., and Fäh, D. (2014). Assessment of Site Effects in Alpine Regions through Systematic Site Characterization of Seismic Stations. *Bulletin of the Seismological Society of America*, 104(6):2809–2826.

Michel, C., Fäh, D., Edwards, B., and Cauzzi, C. (2017). Site amplification at the city scale in Basel (Switzerland) from geophysical site characterization and spectral modelling of recorded earthquakes. *Physics and Chemistry of the Earth, Parts A/B/C*, 98:27–40.

Park, C. B., Miller, R. D., and Xia, J. (1999). Multichannel analysis of surface waves. *Geophysics*, 64(3):800–808.

Poggi, V., Edwards, B., and Fäh, D. (2011). Derivation of a Reference Shear-Wave Velocity Model from Empirical Site Amplification. *Bulletin of the Seismological Society of America*, 101(1):258–274.

Poggi, V., Edwards, B., and Fäh, D. (2012a). Characterizing the Vertical-to-Horizontal Ratio of Ground Motion at Soft-Sediment Sites. *Bulletin of the Seismological Society of America*, 102(6):2741–2756.

Poggi, V. and Fäh, D. (2010). Estimating Rayleigh wave particle motion from three-component array analysis of ambient vibrations. *Geophysical Journal International*, 180(1):251–267.

Poggi, V., Fäh, D., Burjánek, J., and Giardini, D. (2012b). The use of Rayleigh-wave ellipticity for site-specific hazard assessment and microzonation: application to the city of Lucerne, Switzerland. *Geophysical Journal International*, 188(3):1154–1172.

Redpath, B. B. (1973). Seismic refraction exploration for engineering site investigations. Technical report, Explosive Excavation Research Laboratory, Livermore, California.

Reynolds, J. M. (2011). *An Introduction to Applied and Environmental Geophysics*. John Wiley & Sons, Ltd.

Roesset, J. (1970). Fundamentals of soil amplification. In Hansen, R. J., editor, *Seismic Design for Nuclear Power Plants*, pages 183–244. M.I.T. Press, Cambridge, Mass.

SIA (2003). *SIA 261 Actions sur les structures porteuses*. Société suisse des ingénieurs et des architectes, Zürich, sia 261:20 edition.

SIA (2014). *SIA 261 Einwirkungen auf Tragwerke*. Société suisse des ingénieurs et des architectes, Zurich, Switzerland.

Socco, L. and Strobbia, C. (2004). Surface-wave method for near-surface characterization: a tutorial. *Near Surface Geophysics*, 2(22):165–185.

Wathelet, M. (2008). An improved neighborhood algorithm: Parameter conditions and dynamic scaling. *Geophysical Research Letters*, 35(9):1–5.